dependent reactions that create the energy rich molecule ATP which is the energy currency of the cell) and protein synthesis[45] are initiated within the tube cell. By 15 minutes, RNA synthesis has begun and, even when this RNA synthesis is blocked experimentally, the germination and early growth of the pollen tube proceeds[46]. This suggests that the RNA required for the early phases of germination and tube growth is preformed in the pollen tube cell and is ready for utilization.

Ultrastructural studies of pollen germination and tube growth show that in the few minutes before emergence of the pollen tube, structures called Golgi bodies are activated. These accept proteins from the endoplasmic reticulum and bundle them into more complicated molecules. These molecules are shipped out (so to speak) in packages called vesicles[47], produced by the Golgi bodies. The vesicles migrate and fuse locally with the pollen tube's boundary layer, called the plasma membrane, to form the growing tip of the pollen tube. As they fuse with the plasma membrane, the vesicles release their contents of cell wall material that contribute to the lengthening pollen tube. They also release enzymes that are believed to help dissolve a pathway for the pollen tube through the stylar tissue of the flower's pistil[48],[49]. The starch and lipid, stored in the amyloplasts and spherosomes, respectively, are presumably utilized as energy sources and provide raw materials for the construction of new cell wall material and new plasma membrane during pollen tube elongation.

When pollen grains of many plants are placed in water for microscopic examination, they often will germinate and form a short tube, but then they frequently rupture, to release the cytoplasmic contents of the tube cell into the water. As the cytoplasmic contents disperse into the water, the more numerous and larger amyloplasts and spherosomes are seen. Other organelles are too small (ribosomes are about .02$\mu$m) to be seen with the light microscope or too few (nucleus) to be easily spotted.

Jost[50] first suggested that, during pollen germination and pollen tube growth, sugar plays the role of osmotically regulating the swelling and bursting of pollen grains and tubes. However, Bilderback[51] demonstrated that the pollen grains of some plants do not require sugar to stabilize pollen growth and tube elongation. Schumucker[52] recognized that boron plays an active role during pollen tube growth. Its physiological behavior remained unknown until Dickinson[53] found that boron binds in a reversible manner to growth-related sites in the pollen tube. Calcium and potassium[54],[55],[56] also have been found to be essential for stable growth of pollen tubes. Weiseseel and Jaffe[57] were able to show that potassium enters the tips of actively growing pollen tubes. The directed growth of the pollen tube to the plant egg may be due to a gradient of calcium, potassium, hydrogen and chloride within the flower's pistil, extending from the stigma to the egg [58],[59]. The details of pollen tube evolution are an active subject of research[60]. Observation of pollen tube growth makes an engaging student lab[61].

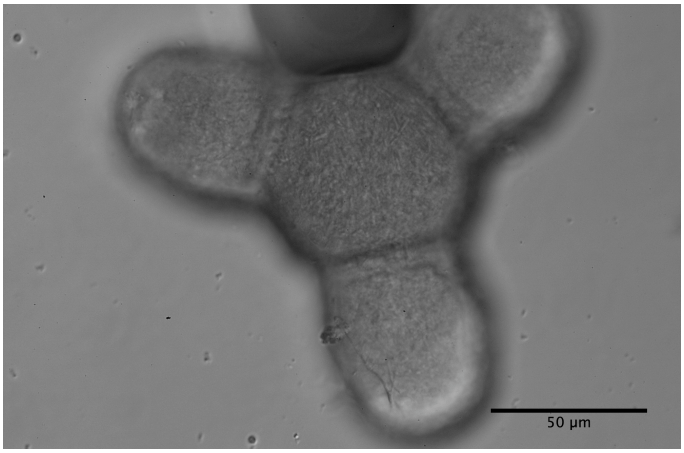


FIG. 3: *Clarkia amoena* pollen under the microscope ×400

Artificial pollen incubation media did not begin to be formulated until the beginning of the twentieth century. Thus, Brown put pollen into water, observed the contents of ruptured pollen grains, and discovered Brownian motion instead of (rediscovering) the pollen tube.

## V. MICROSCOPY

As mentioned in the Introduction, this section is written in the first person.

*Clarkia pulchella*, variously called ragged robin, elkhorn, pinkfairies and deerhorn (because of its four three-pronged petals), is native to western North Amer-

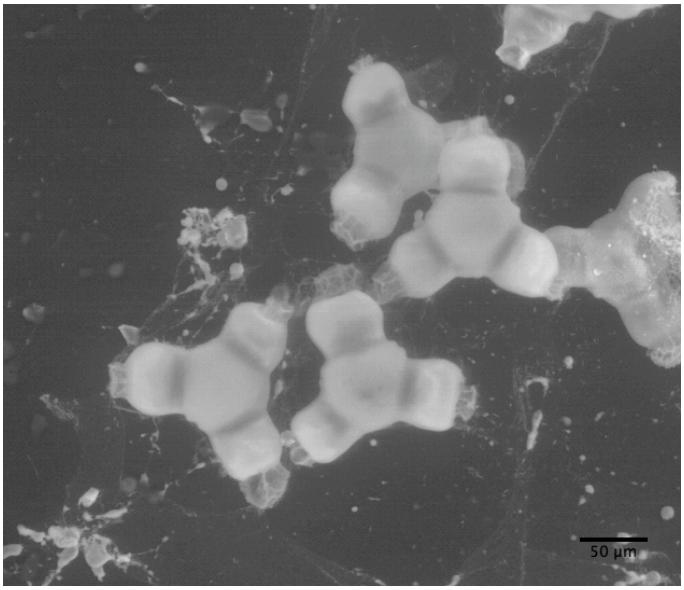


FIG. 4: *Clarkia elegans* pollen under the electron microscope.

ica. It can be found growing wild in parts of British Columbia, Idaho, Montana, South Dakota and Washington[62]. Indeed, I observed some sent to me that grew wild near Missoula, Montana. However, a number of companies sell *Clarkia pulchella* seeds[63], along with seeds of *Clarkia amoena* (also called farewell-to-spring), which grows wild in California, Oregon and Washington, and seeds of *Clarkia elegans* (also called unguiculata, mountain garland) which grows wild in California. Seed packets sell for just a few dollars. (Other *Clarkia* species, of which 41 are known[64], are sold less frequently).

### A. Growing *Clarkia*

Seed–growing advice is available on–line and in many gardening books. Growing seeds indoors under lights is not hard. Here is one person's experience, which certainly can be improved upon. My aim was to do as little as possible.

There are many seed growing systems available at gardening stores, such as peat pots. I have had good results with the Lee Valley Self-Watering Seed Starter[65], which contains 24 compartments, watering via a felt capillary mat, and a water level indicator. It can be left for about a week before refilling with water. The mat should be soaked before using. Lee Valley recommends using a soilless mixture containing sphagnum or peat, but I used a commercial potting soil mix with added nutrients.

A shop light fixture with grow–light bulbs, or even ordinary fluorescent bulbs, can be used, with some arrangement to raise the plants or lower the light fixture. However, I used a commercial stand with grow–lights which is reasonably priced[66] and has a mechanism for raising and lowering the fixture. A timer that kept the lights on perhaps 16 hours a day completed the equipment.

Seeds may be meted out to the compartments from the seam of a small folded piece of paper. The seeds germinated in about a week to ten days. The bulbs should be within a few inches of the tops of the plants, else the plants become etoliated, i.e., spindly from lack of sufficient light. After a few weeks to a month, I transferred the seedlings to 4" pots, 24 of which fit in a tray (periodically watered)[65]. As the plants grew, I staked them. Flowers started to bloom after about ten weeks.

### B. Qualitative

*C. pulchella* has four stamens (eight for *elegans* and *amoena*) surrounding the pistil. I used a miniature Swiss army knife scissors (a nail scissors will do as well) to cut each filament so the anther fell on a microscope slide. I used tweezers to hold an anther. If the anther had not yet burst, I sliced it with a long sharp sewing needle to reveal the pollen. If it had burst, usually some pollen had fallen out of the anther and was already on the slide. In either case, I scraped pollen out of the anther with the needle. I enjoyed observing what I was doing through a low power binocular microscope, though this can be done without one. *C. pulchella* pollen are little triangles, which glowed in the light like diamonds.

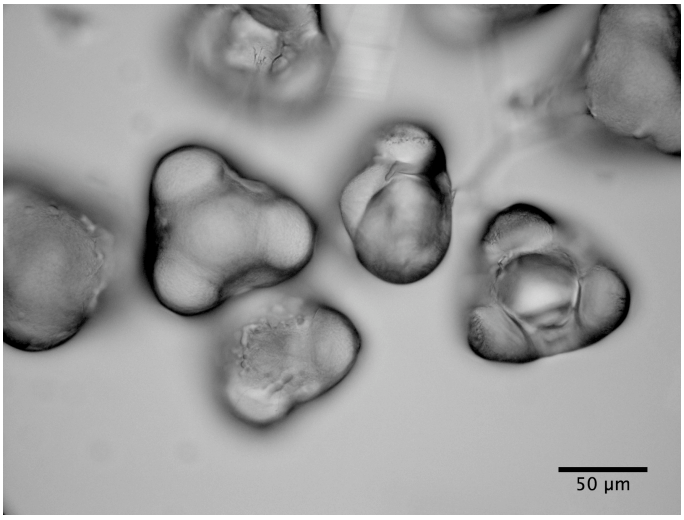


FIG. 5: Desiccated *Clarkia pulchella* pollen

I was surprised when I did the same with *C. amoena* and *C. elegans*. I had not known that species of the same genus could have differently shaped pollen, in this case hexagons with protuberant lobes on alternate edges (Figures 3 and 4). The connection between the two shapes is apparent (see Figure 5) when viewing a dry slide of desiccated *C. pulchella* pollen. Each appears as a membrane surrounding the *C. amoena/C. elegans* pollen shape.

A drop of distilled water is put on the pollen on the slide using a medicine dropper, followed by a cover slip and then observed. One should follow Brown's injunc-

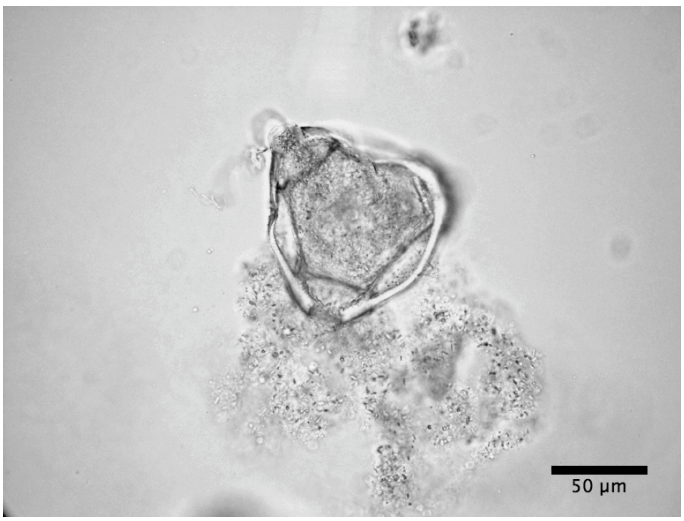


FIG. 6: Bursting *Clarkia pulchella* pollen.

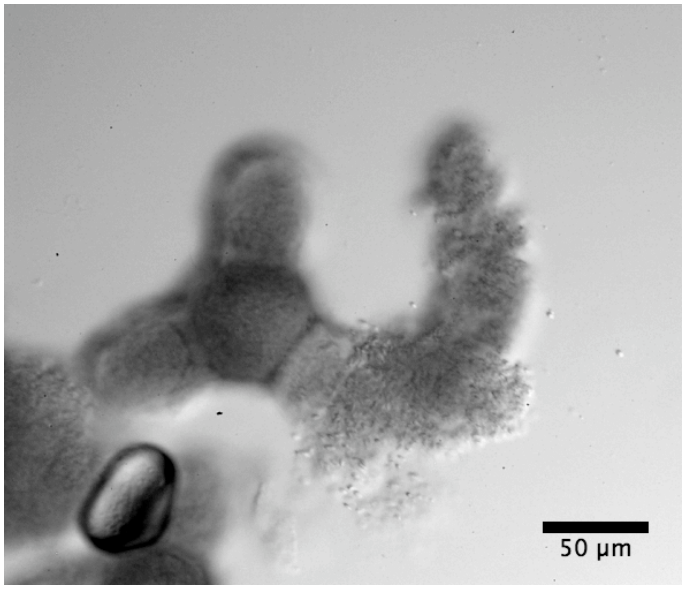


FIG. 7: Bursting *Clarkia elegans* pollen.

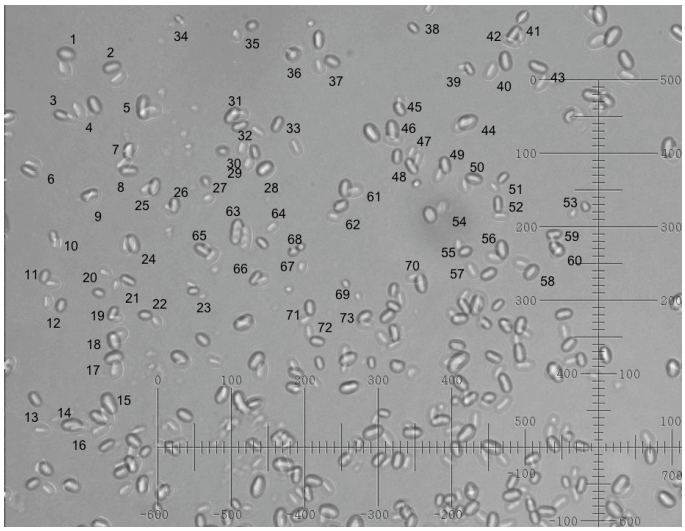

FIG. 8: *Clarkia pulchella* pollen contents before dehiscence, two superimposed photos taken 1 min apart, at ×400. The scale is 2 $\mu$m per division.

tion to observe pollen from anthers either before dehiscence (i.e., before the anther has split open, releasing the pollen) or soon thereafter. Most of the pollen do not burst in water, and if one waits too many days after dehiscence to make observations, none may burst, especially for *C. pulchella*. As pollen matures in the anther, its outer membrane may grow more impervious to bursting in water.

When first viewed, particles from the pollen were sometimes seen already on the slide: perhaps the pollen had been damaged by the needle, or the pollen had rapidly burst open as soon as the water was applied. I could also see pollen bursting before my eyes, and the particles streaming out (Figures 6, 7), like logs released from a log–jam, usually in fits and starts. The particles at the log–jam periphery diffuse away from the rest and can be seen undergoing Brownian motion. The remainder are packed closely, and the intracellular medium in which they sit is viscous, so they show little or no Brownian motion until the log–jam disperses.

### C. Quantitative

There are many interesting phenomena one can investigate. Here are two brief studies, suggestive but by no means definitive. For the first, we consider the distribution of particle sizes emerging from *Clarkia pulchella* pollen before and after dehiscence. For the second, we consider Brownian motion and Brownian rotation of the amyloplasts.

#### *1. Observations*

An Olympus BX-50 microscope, at ×400 was used. Its resolution is cited as .45 $\mu$m, and its depth of focus as 2.5 $\mu$m. A microscope camera and five different computer applications were employed,.

Fig. 8 shows two superimposed photos of *C. pulchella* particles taken 1 minute apart, from pollen *before* dehiscence. The two pictures were enhanced in contrast and treated differently in brightness and then superimposed, using the program Photoshop Elements 2. A marvelous free program, called ImageJ[67], enables precision measurements on photographs. 73 particles in the upper left quadrant of the viewing area (two time-displaced images of each) were labeled. Each image's long axis length, long axis angle $\theta$, $x$ and $y$ coordinates were measured. ImageJ puts the results in an Excel worksheet.

Fig. 9 shows a photo of *C. pulchella* particles from pollen *after* dehiscence. 89 particles in the lower left quadrant were labeled and their lengths were measured. A graph of number of particles per radius bin (radius $R \equiv 1/2\times$particle length, bin size =.25 $\mu$m) for both photos appears in Fig. 10.

Qualitatively, this confirms what Brown said. There are very few spherosomes visible in Fig. 8, taken from pollen before dehiscence. The appearance after dehiscence, in Fig. 9, of many particles of apparent radius $\lesssim$ 1$\mu$m, the "molecules," or spherosomes that so excited Brown, is strikingly apparent. These particles appear as light or dark, depending upon their location with respect to the microscope focal plane.

Fig. 10 presents a graph of what is observed in Figs. 8, 9. The distribution of numbers of particles with radii above 1 $\mu$m before and after dehiscence appears to be the same: these are the amyloplasts. However, there is a peak in the number of particles with radii less than 1 $\mu$m

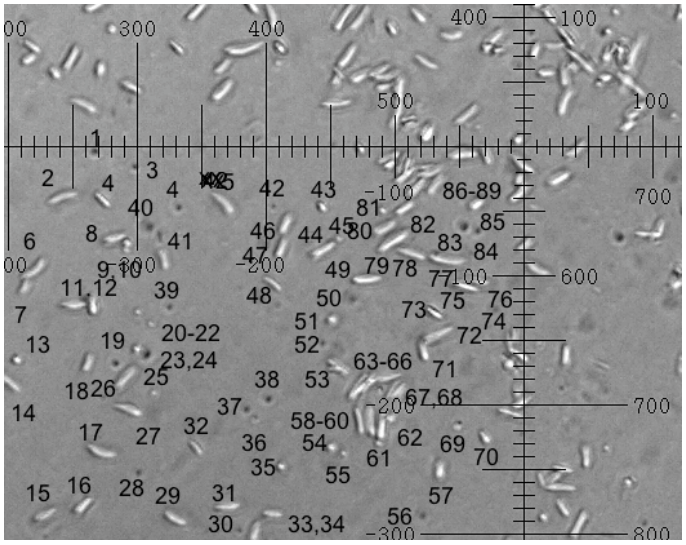

FIG. 9: *Clarkia pulchella* pollen contents after dehiscence. The scale is 2 $\mu$m per division.

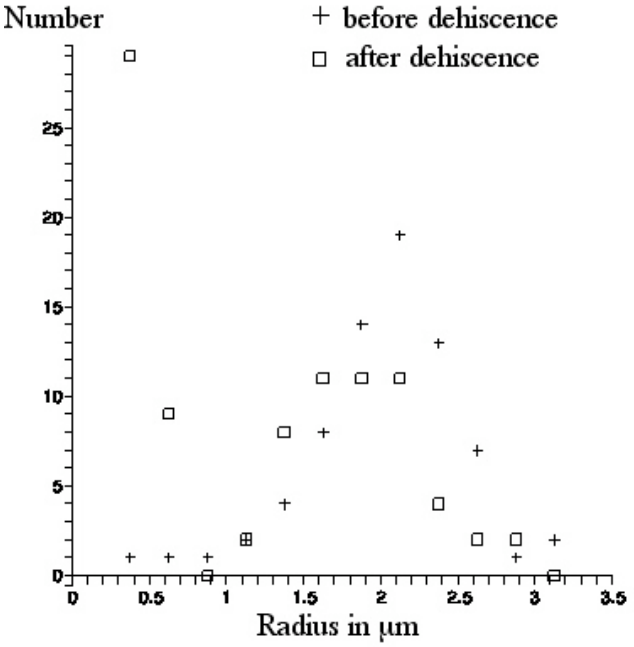


FIG. 10: Number of particles (in a radius bin .25 $\mu$m wide) vs radius in $\mu$m.

after dehiscence (and no such peak before dehiscence): these are the spherosomes.

Quantitatively, there is a discrepancy between Brown's observation of the sizes of the amyloplasts and spherosomes, and what is depicted here: his sizes are larger. As we have noted, Brown quotes the amyloplasts as having average radius (half the long axis length) $R \approx 3$ $\mu$m, with maximum $R \approx 4$ $\mu$m, whereas with our Olympus microscope, on average $R \approx 2$ $\mu$m, with maximum $R \approx 3$ $\mu$m. And, he quotes the spherosome radii as ranging from $R \approx .65$ $\mu$m to $R \approx .85$ $\mu$m, whereas with our Olympus microscope, most spherosomes appear to cluster around $R \approx .5 \pm .05$ $\mu$m, with maximum size about $R \approx .65 \pm .05$ $\mu$m.

To resolve this discrepancy in the case of the spherosomes, in section V C 2 below, lenses and their effect on the image of a round object are discussed. Essentially, due to diffraction, Brown's lens and the Olympus microscope both enhance the image beyond the actual size of the object, but the Olympus microscope enhances the image less than did Brown's microscope. The theory, described in section V C 3, is found to be in good agreement with observations, of polystyrene spheres of known radius, made with the Olympus microscope. Therefore, in section V C 4, the theory is applied to observations of spherosomes with the Olympus microscope, enabling estimation of the spherosome size. Then, Brown's observations of the spherosome size enables estimation of properties of his microscope!

Section V C 5 treats the Brownian motion and rotation evinced in Fig. 8.

Lastly, in section V D, the construction of a ball lens microscope with power close to that of Brown's lens is presented. Aided by a picture of amyloplasts taken with it, the amyloplast size discrepancy is discussed.

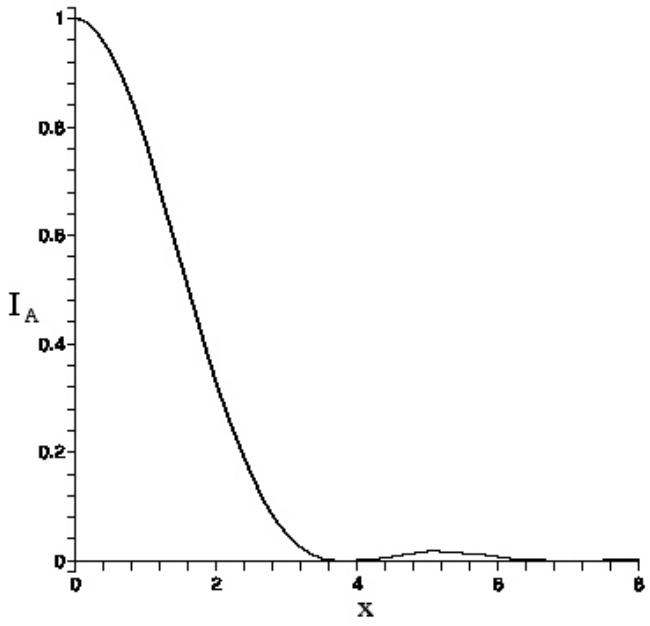


FIG. 11: Airy function intensity $I_A(x)$ vs $x$.

### 2. Lenses

Interestingly, Brown's hypothesis and conclusion, of the ubiquity and uniformity of the "molecules," although wrong, was so stimulating to him that it led to his famous discovery. As mentioned in the Introduction, when he was viewing objects smaller than the resolution of his lens, diffraction and possibly spherical aberration produced a larger, uniform, size[68].

We now discuss this further, summarizing mathematical results given in Appendices F, G. The main result is Fig. 12, which will enable us to find the radius $a$ of a spherical object from the larger radius $R$ of the image observed through a lens or microscope. The theory shall be compared to observations of polystyrene spheres made with the Olympus microscope. Then, the results shall be applied to the spherosome size discrepancy .

Also, using these ideas, we shall attempt a bit of historical detective work. From information supplied by Brown about the size of his "molecules," we can hazard a guess at the radius $b$ of the circular aperture that backed his microscope lens, which is called the exit pupil.

For sufficiently small $b$, a point source of light's image is a diffracted intensity distribution, a circular pattern of light. The intensity as a function of radial distance $r$ from the lens axis is given by the Airy function, Eq. (F5):

$$I_A(x) = \left[\frac{2J_1(x)}{x}\right]^2, \tag{3}$$

where $J_1(x)$ is the Bessel function and $x \equiv krb/f$. Here, f is the lens focal length and $b/f$ is called the "numerical aperture" of the lens. $k = 2\pi/\lambda$, where $\lambda$ is the wavelength of the light, traditionally taken for design purposes as green light with $\lambda = .55$ $\mu$m. This expression (and those which follow, such as Eq. (4)) give properly scaled dimensions of the image. Dimensions actually seen through the lens are larger by a factor of the lens magnification.

The Airy function (3) is graphed in Fig. 11. The intensity vanishes at the first zero of the Bessel function, $J_1(3.83...) = 0$. This defines the Airy radius $r_A$. Setting $kr_Ab/f = 3.83$ allows one to find the lens's Airy radius:

$$r_A = \frac{.61\lambda}{b/f}. \tag{4}$$

Since viewing is subjective, the Airy radius (4) may not be perceived as the boundary of the Airy pattern light intensity (the so-called "Airy disc"), but it is not far off. For consistency with the non–Airy intensity pattern that appears as $b$ is increased, which also fall off rapidly with distance but does not vanish, we shall define the light boundary as occurring at 5% of peak value. Applied to the Airy function, since $I_A(3.01..) = .05$, this criterion puts the radius of the light boundary at $R \equiv (3.01/3.83)r_A \approx .8r_A$.

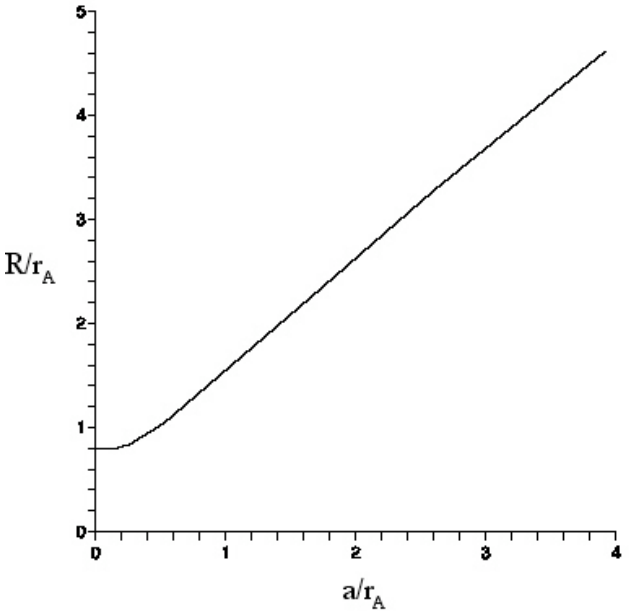


FIG. 12: For an object hole of radius $a$, R is the image circle's radius, defined as where the intensity is 5% of the intensity at the center of the image circle. $r_A$ is the Airy radius.

As $b$ grows, according to Eq.(4), the Airy radius $r_A$ diminishes: this increases resolution. Moreover, as the aperture grows, more light exits the lens: this increases visibility. However, eventually as $b$ is increased further, visibility and resolution start to decrease. The light intensity outside $r_A$ grows, and light intensity inside $r_A$ decreases. This is due to spherical aberration: rays at the outer edge of the exit pupil come to a focus closer to the lens than do paraxial rays. A design choice, called the Strehl criterion[70], suggests an optimal choice of $b$ which keeps spherical aberration at a tolerable minimum while maximizing visibility: the intensity on the optic axis (in the image plane that minimizes the observed disc radius) should be 80% of $I_A(0)$ . The intensity shape is then still close to the Airy distribution. In this case, the image is described as "diffraction limited": this shall be assumed hereafter.

Consider now, instead of a point source, an extended object, modeled by a hole of radius $a$ illuminated by incoherent light. In geometrical optics, for *an ideal lens*, each point on the object plane is imaged onto a point on the image plane. Therefore, there will be a circular image which appears also to have radius $a$. But, with *an actual lens*, each point in the object plane becomes an Airy disc in the image plane. These discs add like little spotlights of radius $r_A$, with centers uniformly distributed throughout a circle of radius $a$. Therefore, the image radius $R$ is larger than $a$.

Fig. 12 graphs $R/r_A$ vs $a/r_A$. This was obtained by numerical evaluation of Eq.(G1), which gives the net in-

tensity of the image pattern at any radius in the image plane. Fig. 12 can be understood as follows.

For small $a$, $a/r_A \lesssim .25$, the centers of the Airy discs that contribute to the intensity are so close together that the intensity is essentially the Airy pattern. Thus, $R/r_A \approx .80$ as discussed following Eq.(4).

As $a/r_A$ grows beyond $\approx .25$, $R$ starts to grow as well, since the Airy disc centers are now spread out over a non-negligible range. For example, we see from Fig. 12, for $a/r_A \approx .5$ that $R/r_A \approx 1$, and for $a/r_A \approx 1$, that $R/r_A \approx 1.5$.

For very large $a/r_A$, the intensity at the center of the image circle is contributed mostly by Airy discs whose own centers lie within an Airy radius of the center. This is true for points somewhat farther out from the center so, at the center and to an extent beyond, the intensity remains essentially constant. But, at distance $a-r_A$ from the center, the intensity starts to drop.

At the "edge" (distance $a$ from the center), the intensity is about half that in the center, because only Airy discs on the inner side of the edge contribute. The intensity drops off further as the distance from the center increases beyond $a$, reaching 5% of $I_A(0)$ at distance $R \approx a + r_A$. Thus $(R-a)/r_A$ asymptotically approaches 1.

In the graph of Fig.12, $R/r_A$ has its largest value for $a/r_A = 4$, at which $(R-a)/r_A \approx .7$. Not shown on the graph are points $\{a/r_A, \approx (R-a)/r_A\} = \{8, .8\}, \{17, .9\}, \{30, .99\}$.

### 3. Polystyrene Spheres

To provide an experimental counterpart to these calculations, slides of .3 $\mu$m and 1 $\mu$m diameter polystyrene spheres[72] ( diameter standard deviation less than than 3%) were prepared and digitally photographed using our Olympus BX-50 microscope, along with a scale whose line spacing is 2 $\mu$m. For this microscope, the manufacturer states the resolution is $r_A = .45$ $\mu$m.

For .3 $\mu$m diameter spheres, since $a = .15\mu$m and so $a/r_A = .33$, we find that $R/r_A \approx .86$ from Fig.12. Therefore, the spheres should appear as of diameter $2R \approx 2(.86r_A) \approx .77$ $\mu$m.

No pictures shall be given here, but the observations are summarized. The digital image was enlarged until it appeared as composed of pixels, each a .2 $\mu$m$\times$.2 $\mu$m square. Spheres which stood alone (for, many spheres cluster) typically appeared as 3×3 pixel grids (dark in the middle, and grey on the outside, with the surrounding pixels lighter and more-or-less randomly shaded), although a 4×4 grid for a few could not be ruled out. Thus the spheres appeared to be of diameter $\approx .6$ $\mu$m, with error of a pixel size, consistent with the estimate.

For 1 $\mu$m diameter spheres, since $a = .5$ $\mu$m and so $a/r_A = 1.1$, we find that $R/r_A \approx 1.7$ from Fig.12. Therefore, the spheres should appear as of diameter $2R \approx 2(1.7r_A) \approx 1.5$ $\mu$m.

In the unenlarged photograph, isolated spheres seemed to be only slightly larger than 1 $\mu$m, perhaps 1.2-1.3 $\mu$m, with a bright center (the spheres are transparent) and dark boundary. However, when enlarged so that the pixels could clearly be seen, particularly the outermost light grey ones, the spheres typically appeared as an 8×8 grid. Thus the spheres appeared to be of diameter 1.6 $\mu$m, with error of a pixel size, consistent with the estimate.

### 4. Spherosome Sizes and Brown's Lens

In the previous section we have seen that the polystyrene sphere sizes observed through our Olympus microscope are larger than the actual sizes . Therefore, we expect the same to be true of the spherosomes. Moreover we expect that the spherosome sizes observed by Brown will be even larger than what we observed, due to a larger Airy radius for Brown's lens than the .45 $\mu$m Airy radius for the Olympus microscope. The universal size of Brown's "molecules," regardless of their source, can be attributed to their being small enough so that their Airy disc is what Brown observed.

We do not have an electron microscope picture of spherosomes to indicate their actual sizes, as that proved to be very difficult to obtain: that is a challenging project for the future. Unlike amyloplasts which are structurally robust and whose electron microscope picture we succeeded in obtaining (see Fig. (16), spherosomes are membrane bound lipid droplets: when an attempt is made to concentrate them by filtering so that there are sufficient numbers to view, they coalesce, and appear as an amorphous mass.)

We therefore turn to estimate the actual spherosome sizes using our observations through the Olympus microscope As we have noted, according to Fig. 10, we observed that most spherosomes appeared to cluster about 1±.1 $\mu$m in diameter, the largest being perhaps 1.3±.1 $\mu$m in diameter.

For the smallest spherosomes, we have $R/r_A \approx (.9/2)/.45 \approx 1$. From Fig. 12 we read that therefore $a/r_A \approx .5$, so their radius is $a \approx .5 \times .45 \approx .2$ $\mu$m, i.e., their diameter is $\approx .4$ $\mu$m.

For most spherosomes, we have $R/r_A \approx (1/2)/.45 \approx 1.1$. From Fig. 12 we read that therefore $a/r_A \approx .6$, so their radius is $a \approx .6 \times .45 \approx .27$ $\mu$m, i.e., their diameter is $\approx .54$ $\mu$m.

For the largest spherosomes, we have $R/r_A \approx (1.4/2)/.45 \approx 1.6$. From Fig. 12 we read that therefore $a/r_A \approx 1.1$, so their radius $a \approx 1.1 \times .45 \approx .5$ $\mu$m, i.e., their diameter is $\approx 1$ $\mu$m.

Armed with these results, we may try to find some properties of Brown's lens. We assume that the minimum size of his "molecules" corresponds to the Airy disc, i.e., they belong in the realm $a/r_A < .3$ in Fig. 12 for which $R/r_A \approx .8$. Since Brown quotes the minimum diameter of his "molecules" as $\approx 1/20,000$ in$\approx 1.3$ $\mu$m, half this is the radius $R \approx .65$ $\mu$m, and so the Airy radius of Brown's

lens is deduced to be

$$r_A = R/.8 \approx .65/.8. \approx .8\ \mu\text{m}.$$

Then, from Eq. (4) we may conclude that the radius of the exit pupil of his $f = 1/32$ in$\approx .8$ mm lens was

$$b = \frac{.61\lambda f}{r_A} = \frac{.61 \times .55 \times .8}{.8} \approx .35 \text{ mm}.$$

As a consistency check, we note that Brown quoted the maximum diameter of his "molecules" as $\approx 1/15,000$ in$\approx 1.7\ \mu$m. Then, $R/r_A \approx (1.7/2)/.8 \approx 1.1$. From Fig.12, we read that this corresponds to $a/r_A \approx .6$. Therefore, we deduce that the actual radius of these largest spherosomes is $a \approx .6 \times .8 \approx .5\ \mu$m. This agrees with the actual radius of the largest spherosomes we observed.

### 5. *Amyloplast Brownian Motion and Rotation*

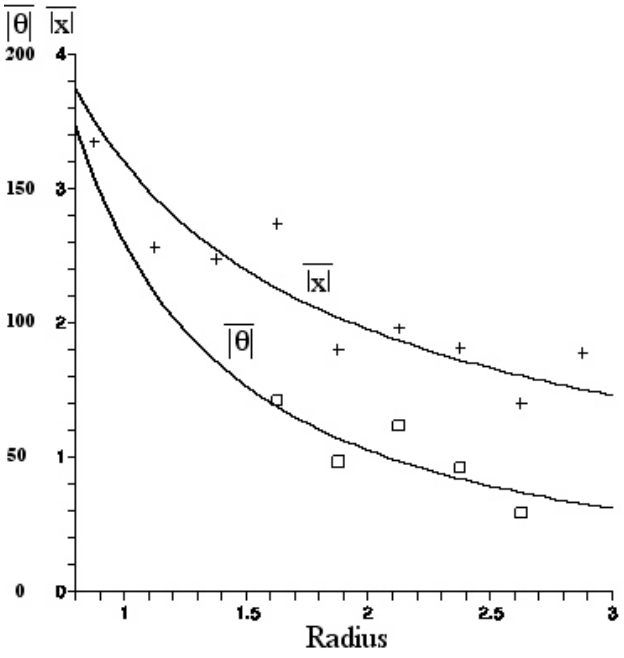


FIG. 13: Mean linear displacement $|\bar{x}|$ in $\mu$m and mean angular displacement $|\bar{\theta}|$ in degrees, vs R in $\mu$m, for amyloplasts undergoing Brownian motion for 60 sec. The least squares fit curves depicted here are given in Eq.(5).

We next turn to analysis of the observed Brownian motion of the amyloplasts. In what follows, $R$ is half the length of the long axis of an amyloplast.

From Fig. 8, the $x$–displacement, $y$–displacement, and $\theta$–displacement of each amyloplast, over the one minute interval, were found. Because of the possibility of overall fluid flow (assumed constant and irrotational in the region containing the observed particles), the mean displacement was calculated; it proved to be .053 $\mu$m in the $x$-direction (negligible flow) and -.847 $\mu$m in the $y$-direction. This was then subtracted from each displacement, to give the true Brownian contribution.

A plot of mean linear displacement and a graph of mean angular displacement for each $R$ bin (.25 $\mu$m wide) appears in Fig. 13. Smallest and largest $R$ values representing too few data points were omitted (which is why there are fewer data points representing $|\bar{\theta}|$ than $|\bar{x}|$). Fig. 13 was made with the Maple program (with labeling help from the Appleworks program), and includes graphs of the least squares fit to a power law $A/R^B$, for each set of data. The results, compared with the predictions given in Eqs. 1, 2 (setting $R_{\text{eff}} \equiv R$) are

$$\begin{aligned} |\bar{x}| &= \frac{3.2}{R_{\mu\text{m}}^{.7}}\mu\text{m} \quad \text{compared with} \quad |\bar{x}| = \frac{4.0}{R_{\mu\text{m}}^{.5}}\mu\text{m}, \\ |\bar{\theta}| &= \frac{130\ ^\circ}{R_{\mu\text{m}}^{1.3}} \quad \text{compared with} \quad |\bar{\theta}| = \frac{201\ ^\circ}{R_{\mu\text{m}}^{1.5}}\ . \end{aligned} \tag{5}$$

The powers in Eqs. (5) agree reasonably well, considering that no correction has been made for the ellipsoidal nature of the particles. As discussed in Section III B and Appendices B 5 and B 9, $R_{\text{eff}}$ for translation and rotation of ellipsoids in Eqs. (1), (2) should be less than $R$ for a sphere by a factor that is different for the long and short axes, and that varies with their ratio. No attempt was made to correct for this effect, nor for the fact that the observed amyloplast sizes are larger than the actual sizes, just as in the case of the spherosomes.

Interesting studies, with appropriate selection of uniform particle sizes, can be made. The subject of Brownian motion of ellipsoids, first studied by Perrin, is still of interest[71].

The numerical coefficients in the comparable Eqs.(5) differ because the last terms on the right–hand sides of Eqs.(1),(2) assume the fluid in which the particles are immersed is water. However, the amyloplasts move in a fluid that is a mixture of water and the intracellular medium, which emerged with the amyloplasts from the pollen. That is, the measured coefficients are proportional to $1/\sqrt{\eta_{\text{fluid}}}$ while the expressions based upon Eqs.(1),(2) are proportional to $1/\sqrt{\eta_{\text{water}}}$. From the displacement expressions in Eq.(5) we obtain for $\sqrt{\eta_{\text{fluid}}/\eta_{\text{water}}}$ the value $(4.0/3.2) \approx 1.3$, while from the angular displacements this is $(201/130) \approx 1.5$. These estimates of the fluid viscosity are in reasonable agreement, especially considering the omission of an ellipsoidal correction mentioned above.

One last qualitative observation is worth mentioning. Some wet-dry 400 grit sandpaper was used to grind to powder some of a seashell, a rock, and a nickel. In all cases, the powder (which was colored white or grey, while the sandpaper was colored black, so the sandpaper grit was not being observed), had some particles of apparent sizes $\lesssim 1\mu$m which were observed jiggling in water, just as Brown said occurred for anything he ground up fine

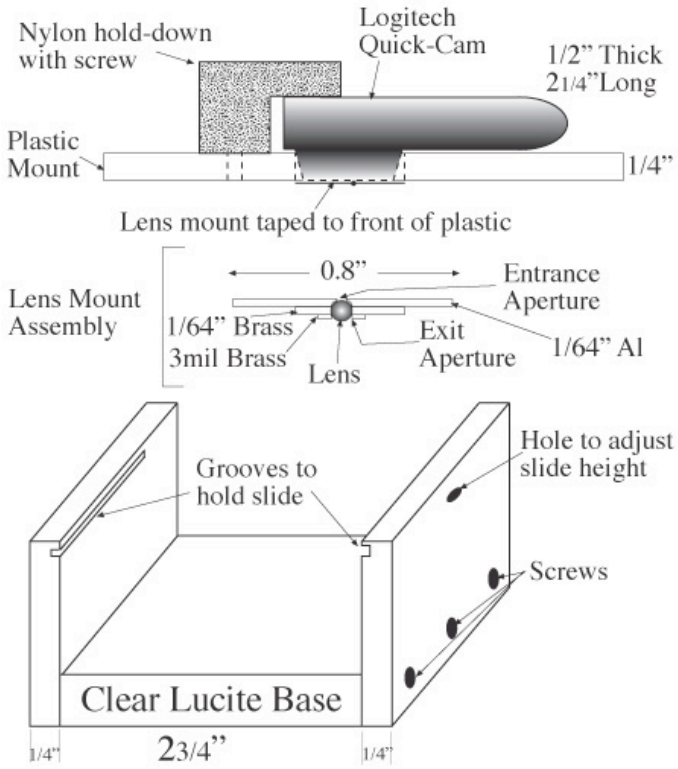


FIG. 14: Ball Lens Microscope Diagram

enough.

### D. Ball Lens Microscope

Finally, we discuss construction of a single lens microscope with a magnification comparable to Brown's, and some observations made with it.

Ground lenses of high magnification such as those made by Bancks and Dollond are not readily available nowadays. However, fortunately, precision small glass spheres called ball lenses are readily available (they are used for coupling lasers to optical fibers) that can be used as high magnification lenses[73]. We purchased a ball lens of 1 mm diameter and index of refraction 1.517[74]. The focal length $f$ of a sphere of radius $R$ can be found from the lensmaker's formula[75] for a thick lens of radii $R_1$ and $-R_2$, thickness $T$ and index of refraction $n$:

$$\frac{1}{f} = (n-1)\Big[\frac{1}{R_1} - \frac{1}{R_2} + \frac{(n-1)T}{nR_1R_2}\Big]. \qquad (6)$$

For $T = 2R$ and $R_1 = -R_2 = R$, Eq. (6) yields

$$f = nR/2(n-1). \qquad (7)$$

For our lens, $f$= .733 mm=1/34.6 inch, not far from the $f$=1/32 inch of Brown's lens.

The "microscope" is essentially the lens sandwiched between two perforated supports. One support was made as follows. A circle of 1" diameter was cut out of a 1/64" (≈0.4 mm) thick aluminum sheet. A 0.8 mm. diameter hole was drilled part way through its center, and then a 0.48 mm diameter hole was drilled all the way through. Thus, the exit pupil radius was constructed to be 0.24 mm. Then, a small washer was made from a piece of 1/64" brass with a 1 mm diameter hole drilled through it. The holes in the two pieces were aligned, and the pieces secured to each other with Kapton polyimide tape. The ball lens was placed in the resulting hole, supported by the edges of the 0.48 mm hole and surrounded by the washer.

The second support consisted of a piece of 3 mil (0.076 mm) brass shim stock with a 0.55 mm diameter hole in the center, It was secured over the lens with more Kapton tape to hold the lens in place and serve as the entrance aperture.

The assembled "microscope" was then mounted with more Kapton tape over the entrance aperture of a Logitech QuickCam Pro USB camera. This camera was chosen from a large number of such "webcams" because the front of its lens lies very close to the surface of the camera, allowing a very small separation between the microscope and the imaging camera. A 1/4" × 3" × 5" plastic sheet was fashioned, and a hole was drilled through its center, through which the microscope backed by the camera lens protrudes: the body of the camera rests upon the plastic. An inverted-L shaped bracket was attached to the plastic sheet to hold the camera .

A U-shaped plastic stand, of dimensions slightly less than 3" (the length of a microscope slide) was constructed from 1/4" plastic. Horizontal grooves (rabbets) to support the slide were cut in the sides of the U just

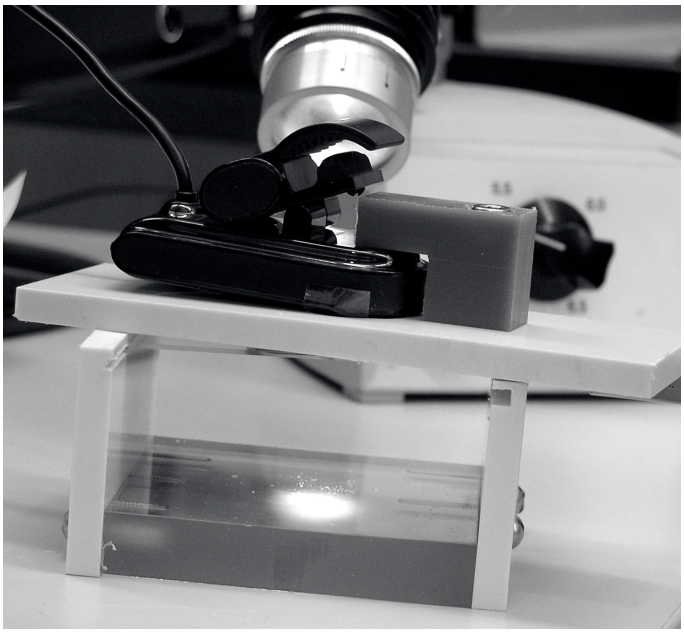

FIG. 15: Ball Lens Microscope Setup.

below the top edges. The plastic sheet holding the microscope/camera rests upon the top edges of the U, and can be moved freely over the slide.

A small hole was drilled through one side of the U, partly through and partly below the rabbet. Focus adjustment is achieved by placing a small wedge (e.g., a toothpick) through the hole and under the slide. As the wedge is moved in and out, it raises and lowers the slide by a fraction of a millimeter. Light from a small microscope illuminator, collimated to a 1" beam, is diffusely reflected from a white surface on which the plastic stand sits, through the slide and into the microscope/camera.

The setup is shown in Fig. 15. The plastic sheet supporting the camera (cable going off to the left) lies in the middle of the picture, slightly skewed to the stand. The ball lens and its support, attached to the camera aperture, lies within a hole in the middle of the plastic sheet, and so is not visible, nor is the focus adjustment hole in the side visible. The inverted L-shaped bracket that affixes the camera, the rabbets which support a slide, and a bit of a slide itself (just below the plastic sheet on the left), the inverted U stand, as well as the light source and its power supply, are visible.

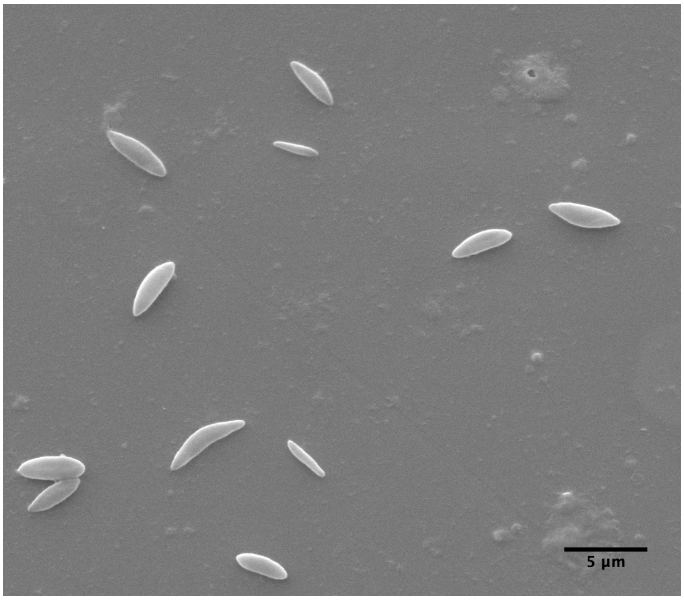


FIG. 16: Clarkia pulchella amyloplasts photographed with the electron microscope.

### 1. *Amyloplasts Seen With Ball Lens Microscope*

Now we address the discrepancy between our observations with the Olympus microscope, summarized in Fig. 10, that the amyloplasts appear to be of average radius (i.e., half-length) $\approx$ 2 $\mu$m, with maximum radius $\approx$ 3 $\mu$m, and Brown's observations with his microscope, that their radius range is $\approx$ 3–4 $\mu$m. We shall do so by showing that the observations with the ball lens are essentially the same as Brown's. But, also, the electron microscope picture Fig.16 of amyloplasts, while not depicting a large sample, suggests that the size distribution measured with the Olympus microscope is reasonably accurate.

For the ball lens, the Airy radius is $r_A = .61\lambda f/b = 1.0$ $\mu$m. This can also be seen in the graph of its intensity versus distance in Appendix F 2, Fig. 20 (the $\bar{B} = 2$ curve). The exit pupil $b$=.24 mm is not the ideal size to minimize spherical aberration according to the Strehl criterion (discussed in Section V C 2 and Appendix F 2). That ideal size is $b$=.19 mm, corresponding to the $\bar{B} = 1$ curve in Fig.20. However, its intensity is still reasonably approximated by the Airy function, so we shall assume that the considerations leading to Fig.12 are valid.

To check that $r_A = 1$ $\mu$m, a slide containing 1 $\mu$m diameter polystyrene spheres was observed and photographed. Another slide containing a scale with marks 10 $\mu$m apart was separately photographed. Both photographs were superimposed using the program Photoshop Elements 2. Using the program ImageJ, the image of the spheres was enlarged so that the pixels could be seen, and they were analyzed, as described for the spheres photographed with the Olympus microscope in section V C 3. The result was that the polystyrene spheres appeared to have diameter 2.1$\pm$.2$\mu$m.

For a theoretical comparison, with $a/r_A = .5/1 = .5$, one reads from Fig. 12 that $R/r_A \approx 1.1$. Therefore, it is predicted that the apparent radius of the spheres should be $R = 1.1r_A = 1.1\mu$m, or diameter 2.2$\mu$m, in good agreement with the observation discussed above.

Now we turn to compare the amyloplast sizes seen with the Olympus microscope and amyloplast sizes seen through the ball lens. Fig. 18 shows a portion of a photo taken through the ball lens, of a slide containing amyloplasts that had emerged from a pollen grain (whose out-of-focus edge appears at the lower left).

As described above, a photograph of a scale was superimposed and the photograph was further enlarged so that pixels were visible. The radius (half the length) of 44 amyloplasts was measured, 14 of which appear in Fig. 18 and 30 appear in another photograph of a different scene. Fig.17 contains a graph of number of amyloplasts in a .25 $\mu$m radius bin versus radius in $\mu$m.

From this graph, the amyloplasts appear through our ball lens as of average radius $\approx$ 3 $\mu$m, with maximum radius $\approx$ 4 $\mu$m. This is $\approx$ 1 $\mu$m larger than what was observed with the Olympus microscope, Fig. 10, but exactly what Brown said about the amyloplast sizes he observed through his lens!

This excellent agreement, between the observations with our ball lens and Brown's observations with his lens should be tempered by the realization that our lens has $r_A \approx 1$ $\mu$m and exit pupil $b$ = .24mm, whereas we have deduced that Brown's lens had $r_A \approx .8$ $\mu$m and exit pupil $b$ = .35 mm. However, it leaves little doubt that Brown was seeing enlarged amyloplasts on account of the diffraction and possible spherical aberration of his lens.

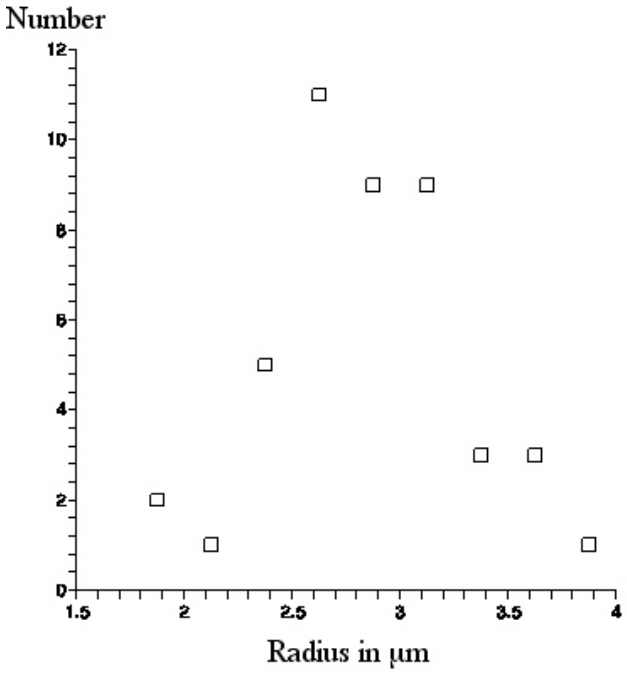


FIG. 17: Number of amyloplasts in a .25 $\mu$m radius bin vs amyloplast radius (= half amyloplast length).

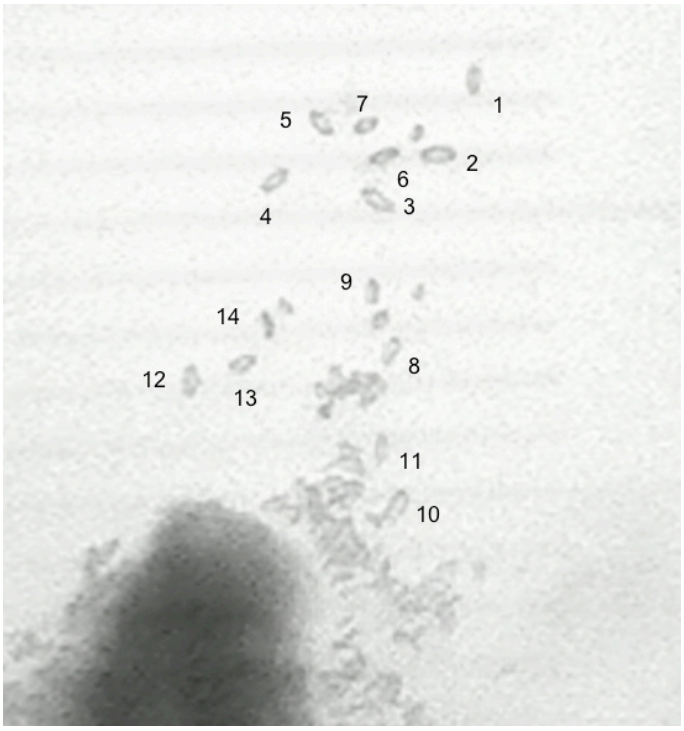


FIG. 18: Amyloplasts photographed with the ball lens microscope. The superimposed scale marks (the faint horizontal lines) are 10$\mu$m apart.

**Acknowledgments**

It is a pleasure to thank Diane Bilderback, Brent Elliot, Brian Ford, Armando Mendez, Michael Milder, Bill Pfitsch, Hilary Joy Pitoniak, Diana Pilson, Bronwen Quarry, James Reveal, Ann Silversmith, Ernest Small, and David Mabberley for help with this endeavor.

## VI. THEORY

The appendices contain seven mathematical tutorials.

Appendix A contains a derivation due to Langevin, of the well known expression, given first by Einstein[76], for the mean-square displacement of an object undergoing Brownian motion[77]. The method is easily applied to give the mean-square angular displacement of an object undergoing Brownian rotation.

These expressions depend upon the viscous force or viscous torque on the object. Such fluid flow analysis is not treated in places which treat the material of Appendix A. The results for a sphere are derived in Appendix B[78]. For an ellipsoid, results are just cited[79].

Appendix C presents a derivation of geometrical optics starting from the wave equation. The discussion here, utilizing the WKB approximation in 3 dimensions, does not seem to be given elsewhere, although the result (the eikonal approximation of geometrical optics) is well known. Appendix D, a digression, applies this result to mirrors and lenses. It is emphasized, because of the approximate solution's abrupt discontinuities at the boundaries of mirrors and lenses, that it must be modified in order to better satisfy the wave equation.

Appendix E contains the modification, obtaining from Green's theorem, in a standard way, the Huyghens-Fresnel-Kirchhoff expression for a diffracted wave emanating a lens[80]. Then, in Appendix F, this theory is used to discuss lens imaging of a point source. Usually, books on optics discuss the diffraction of a lens (due to its limited aperture) and the spherical aberration of a lens (due to the image made by rays at the rim of the lens having a different focal plane than the image made by near-axial rays) separately. Then, no expression is given for their combined intensity. Here, diffraction and spherical aberration receive a unified treatment. As a concrete example, the theory is applied to what is seen through a 1mm diameter ball lens used as a microscope. The optimum choice for the exit pupil for such a lens, to minimize spherical aberration, is discussed.

Appendix G applies these results for a point source to an extended light source, an illuminated hole of radius $a$. The apparent radius of the image is discussed, for small and large $a$. As discussed in section III H, results are obtained which illuminate (sic) Brown's observations of "molecular" size,